NANO LETTERS
Cite This: Nano Lett. 2018, 18, 491−497
Letter
pubs.acs.org/NanoLett

Tunneling Hot Spots in Ferroelectric $SrTiO_3$

Haidong Lu,[†] Daesu Lee,[‡] Konstantin Klyukin,[§] Lingling Tao,[†] Bo Wang,[∥] Hyungwoo Lee,[‡] Jungwoo Lee,[‡] Tula R. Paudel,[†] Long-Qing Chen,[∥] Evgeny Y. Tsymbal,[†,⊥] Vitaly Alexandrov,*[,§,⊥] Chang-Beom Eom,*[,‡] and Alexei Gruverman*[,†,⊥]

[†]Department of Physics and Astronomy, University of Nebraska, Lincoln, Nebraska 68588, United States
[‡]Department of Materials Science and Engineering, University of Wisconsin-Madison, Madison, Wisconsin 53706, United States
[§]Department of Chemical and Biomolecular Engineering, University of Nebraska, Lincoln, Nebraska 68588, United States
[∥]Department of Materials Science and Engineering, Pennsylvania State University, University Park, Pennsylvania 16802, United States
[⊥]Nebraska Center for Materials and Nanoscience, University of Nebraska, Lincoln, Nebraska 68588, United States

Supporting Information

ABSTRACT: Strontium titanate ($SrTiO_3$) is the "silicon" in the emerging field of oxide electronics. While bulk properties of this material have been studied for decades, new unexpected phenomena have recently been discovered at the nanoscale, when $SrTiO_3$ forms an ultrathin film or an atomically sharp interface with other materials. One of the striking discoveries is room-temperature ferroelectricity in strain-free ultrathin films of $SrTiO_3$ driven by the Ti_{Sr} antisite defects, which generate a local dipole moment polarizing the surrounding nanoregion. Here, we demonstrate that these polar defects are not only responsible for ferroelectricity, but also propel the appearance of highly conductive channels, "hot spots", in the ultrathin $SrTiO_3$ films. Using a combination of scanning probe microscopy experimental studies and theoretical modeling, we show that the hot spots emerge due to resonant tunneling through localized electronic states created by the polar defects and that the tunneling conductance of the hot spots is controlled by ferroelectric polarization. Our finding of the polarization-controlled defect-assisted tunneling reveals a new mechanism of resistive switching in oxide heterostructures and may have technological implications for ferroelectric tunnel junctions. It is also shown that the conductivity of the hot spots can be modulated by mechanical stress, opening a possibility for development of conceptually new electronic devices with mechanically tunable resistive states.

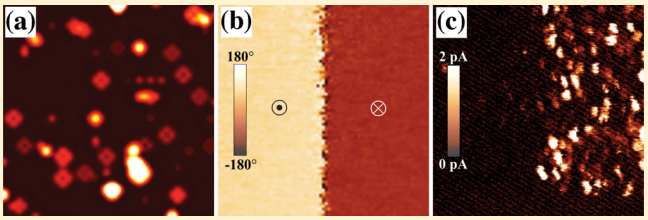

KEYWORDS: *Strontium titanate, resistive switching, ferroelectric, tunnel junctions*

Control of the electrical resistance of complex oxide materials by external stimuli has attracted considerable attention due to potential application in resistive random access memories (RRAM), which can overcome the scaling limitations of memory devices based on charge storage.[1−3] The underlying physical mechanisms of resistive switching (RS) in complex oxides are manifold and, depending upon the type of material, electrodes, voltage range, and environmental conditions, may involve formation of the conducting filaments, interface Schottky barrier modulation, ion migration, and electrochemical redox reactions.[4,5] Recently demonstrated resistive switching, tunneling electroresistance (TER) effect, in ferroelectric tunnel junctions (FTJs) is based on a pure electronic mechanism associated with a change in transmission probability of the tunneling electrons upon polarization reversal due to the modification of the tunneling barrier profile.[6−8] Conventional FTJs exhibit a uniform resistance change over its working area giving rise to a bistable resistance device. On the other hand, resistive switching associated with the chemical or structural disorder in the ferroelectric barrier is highly localized. These local defects could play an important role in the resistive switching of the FTJs by affecting the electron tunneling process thereby allowing a variable resistance change. Investigation of an interplay between these two mechanisms is of great importance as it may allow significant enhancement of the FTJs functional performance.

A prototypical perovskite $SrTiO_3$ (STO) is one of the best-studied complex oxide materials exhibiting resistive switching and can be considered as a model system for investigation of this phenomenon. It has been proposed that in STO this effect is due to the electrically induced variations in oxygen concentration along the extended defects, such as dislocations, leading to a formation of conducting filaments.[9] Recently, emergence of room-temperature ferroelectricity in strain-free ultrathin $SrTiO_3$ films has been reported.[10] In Sr-deficient STO films, the antisite Ti_{Sr} defects (where Ti substitutes Sr) form during growth inducing a sizable local dipole moment by an off-centering displacement and coherently polarizing the surrounding regions. These Ti_{Sr} antisite defects are also known to produce localized states in the band gap of $SrTiO_3$.[11,12] Such

Received: October 18, 2017
Revised: December 6, 2017
Published: December 13, 2017

DOI: 10.1021/acs.nanolett.7b04444
Nano Lett. 2018, 18, 491−497

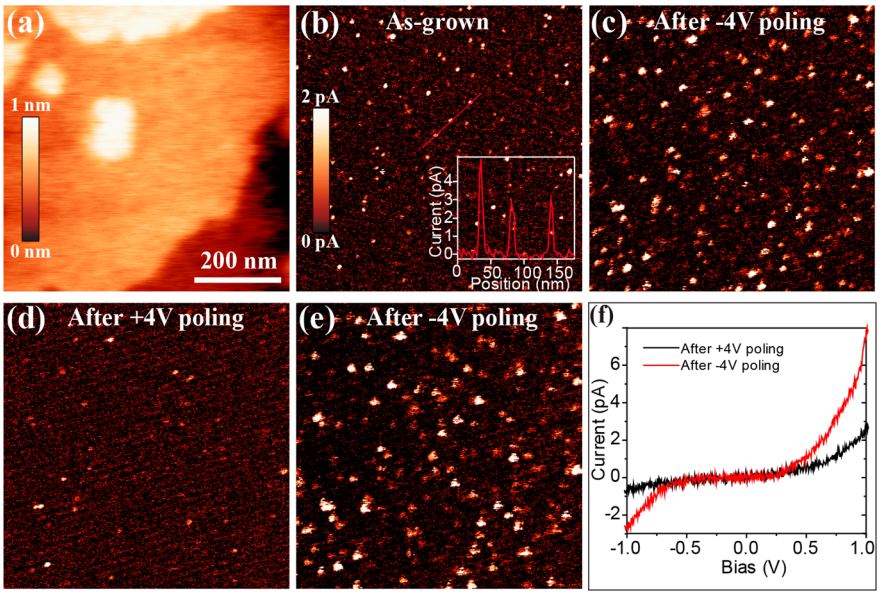

Figure 1. C-AFM mapping of the 12 u.c. thick $SrTiO_3$ film. (a) An AFM image of the surface topography. (b) C-AFM image of the same area of the as-grown $SrTiO_3$ film as in (a) showing randomly scattered conducting paths ("hot spots"). An inset in (b) shows a cross-sectional current profile along the red line revealing a lateral dimension of the "hot spots" of about 10 nm. (c–e) C-AFM images of the same film area after (c) −4 V poling, (d) after +4 V poling, and (e) after −4 V poling again. The "hot spots" appear at the same locations upon repeated application of a positive bias. (g) The *I*–*V* characteristics measured at the same conductive path after ±4 V poling.

localized states may influence currents across the ultrathin STO films through the mechanism of resonant tunneling, where the transmission coefficient peaks at the energy of the localized state.[13] Unlike in the case of direct tunneling in the conventional FTJs with a spatially uniform barrier, resonant tunneling probability relies on the distribution of the defect states in the barrier.

In this paper, we investigate the defect-assisted electroresistance effect in strain-free ferroelectric $SrTiO_3$ thin films. A combination of conductive atomic force microscopy (C-AFM) and piezoresponse force microscopy (PFM) has been used to map spatial variations in electrical current along with measurements of the local current–voltage characteristics as a function of the film polarization state. It has been found that the transport properties of the local conducting paths, "hot spots", formed by the Ti_{Sr} antisite defects widely present in the $SrTiO_3$ films, can be modulated by ferroelectric polarization switching induced both by electrical fields and mechanical forces. Our finding indicates that defect-assisted tunneling may play an important role in predicting the properties of the FTJs and designing the resistive switching devices with improved functionality.

In this study, we have used ultrathin strain-free $SrTiO_3$ films with a thickness of 12 unit cells (u.c.) (~4.8 nm) epitaxially grown by pulsed laser deposition (PLD) on the (001) $SrTiO_3$ substrates with an $SrRuO_3$ buffer layer as a bottom electrode. Details of the sample preparation method can be found in Materials and Methods. Figure 1a,b shows high-resolution topographic and C-AFM images, respectively, of the as-grown $SrTiO_3$ film. The C-AFM image reveals a number of randomly distributed bright spots of about 10–20 nm in size that are not correlated with surface topography. These bright spots correspond to the conducting paths ("hot spots") with a typical current level of a few pA at 1 V bias (inset in Figure 1b), while the background shows a current level below a noise level (~0.2 pA). Noteworthy, the density of hot spots and the estimated current density decreases exponentially as the film thickness increases (there are almost no detectable conducting paths in the films with thicknesses above 36 u.c (see Figures S1 and S2 in Supporting Information)), giving a strong indication of the tunneling conduction mechanism.

To investigate the effect of polarization on the resistive properties of the $SrTiO_3$ films, we performed the electrical poling to the downward (or upward) polarization state by scanning the film surface with +4 V (or −4 V) dc bias applied to the tip followed by C-AFM imaging of the poled regions. The C-AFM images in Figure 1c,d corresponds to the current maps for the downward and upward polarized domains, respectively. It can be seen that the region polarized downward exhibits a much larger number of the hot spots (Figure 1c) than the region polarized upward (Figure 1d). Furthermore, these changes are completely reversible and reproducible, that is, repeated application of the positive bias to the film polarized upward leads to the appearance of conducting paths at the very same locations (Figure 1f), indicating that the hot spots are related to the local immobile defects. Interestingly, polarization reversal leads not only to a significant change in the distribution density of the hot spots but also to their brightness, indicating a change in their conductivity. This effect is evident from the current–voltage (*I*–*V*) curves for opposite polarization states obtained at the same hot spots (Figure 1f). We note that the resistance change of the surrounding matrix upon polarization reversal is much smaller than that at the hot spots (see Figure S3 in Supporting Information) due to a small value of polarization in the $SrTiO_3$ films.[10] In view of this drastically different behavior, the *I*–*V* curves obtained with the probing tip in contact with the top Pt/Co electrode, which shows a clear signature of the resistive switching effect, should be attributed to the predominant contribution of the a number of hot spots (Figure S3 in Supporting Information). This integral effect allows detection of resistive switching in the Pt/Co/$SrTiO_3$/$SrRuO_3$ junctions even in the low voltage range (below 0.3 V),

DOI: 10.1021/acs.nanolett.7b04444
Nano Lett. 2018, 18, 491–497

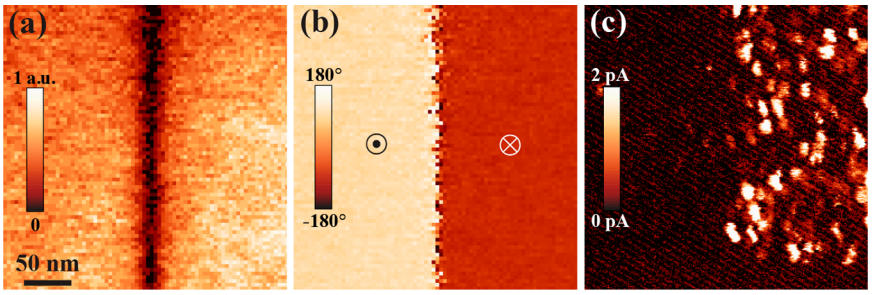

Figure 2. High-resolution PFM and C-AFM imaging on the bipolar domain pattern of the 12 u.c. thick $SrTiO_3$ film. (a) PFM amplitude, (b) PFM phase, and (c) C-AFM images of the bipolar domains generated by scanning the film surface with a tip under ±4 V bias (left half polarized up; right half down). It can be seen that the conductivity of hot spots is modulated by electrical poling.

which is not possible for an individual hot spot due to system sensitivity limitation (Figure 1f).

Figure 2 presents a more direct illustration of the relationship between the polarization state and electrical resistance of the $SrTiO_3$ films. High-resolution PFM images of a bipolar domain structure generated by ±4 V poling reveal uniform amplitude and phase contrast on both sides across the 180° domain wall whereas the corresponding C-AFM image (Figure 2c) shows a completely different pattern: there are randomly scattered "hot spots" in the downward domain area and noise-level variations of the current in the upward domain.

Our earlier results obtained for the same $SrTiO_3$ films showed that a minute amount of Sr defficiency (~1 atomic %) present in those films could generate polar nanoregions (PNRs) without compromising crystalline quality of the films and give rise to the stable room-temperature ferroelectric state.[10] The ferroelectricity is driven by the Ti_{Sr} antisite defects, which produce a polar displacement between Ti and O ions polarizing the surrounding region. Here, we argue that the same type of defects may lead to the appearance of the observed hot spots with higher conductance than the surrounding matrix. Specifically, the localized states generated by the Ti_{Sr} antisite defects may lead to defect-assisted tunneling enhancement. If such states are randomly distributed over the tunneling barrier, the conductance distribution will appear in the form of scattered hot spots associated with the resonant states in the barrier.[14,15] Even more importantly, if the barrier layer is ferroelectric the energy position of the localized states shifts with respect to the Fermi level due to the depolarizing field. Thus, polarization reversal is expected to change the resonant transmission amplitude and, hence, the conductance of a hot spot.

To elaborate on this scenario, we performed theoretical modeling (i) to demonstrate the formation of the localized Ti_{Sr} antisite defect states in the band gap of $SrTiO_3$ in a representative FTJ structure, (ii) to analyze the effect of ferroelectric polarization on the energy position of these states; and (iii) to illustrate the role of hot spots in the polarization-dependent conductance resulting from resonant tunneling through the localized defect states.

In addressing (i), we carried out the density-functional-theory (DFT) calculations (see Materials and Methods for details) using a 5 u.c. thick $SrTiO_3$ (001) layer with Ti_{Sr} defects in it, as shown in Figure 3 (top and bottom panels). The $SrTiO_3$ was placed between two metal (Pt) layers, which modeled the bottom electrode and the tip in our experimental conditions. To emulate the asymmetry of the structures tested experimentally, we introduced asymmetry through the asymmetrical placement of the antisite defects. Asymmetric position of the Ti_{Sr} defect state in the $SrTiO_3$ layer provides asymmetry in the electrostatic potential energy profile (middle panel in Figure 3a). Polarization reversal is associated with the switching of the electrical dipole intrinsic to the Ti_{Sr} defect, resulting in the reversal of the electrostatic potential step at the defect position in $SrTiO_3$. Analysis of the electronic structure based on the layer-resolved density of states (DOS) shows the presence of the localized states below the conduction band minimum of $SrTiO_3$ (Figure 3b) consistent with the previous theoretical calculations.[11,12] The observed two peaks in the DOS of the gap states are associated with the t_{2g}-e_g splitting of the Ti-3d orbitals hybridized with the O-p orbitals on the Ti_{Sr} defect site. The presence of such defect states positioned close to the Fermi energy is expected to assist the conductance through a resonant tunneling mechanism. With respect to (ii) above, from Figure 3b it is evident that, depending on polarization direction,

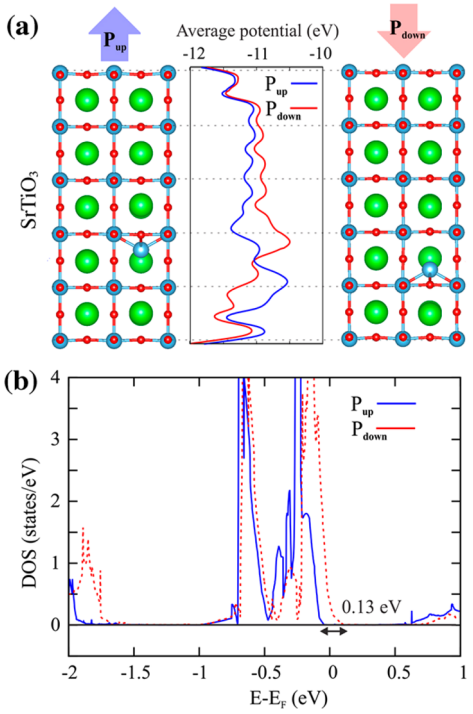

Figure 3. Results of first-principles calculations of ferroelectric $SrTiO_3$ with a Ti_{Sr} defect. (a) Atomic structure of $SrTiO_3$ (001) and the electrostatic potential profile for opposite polarization states (P_{up} and P_{down}) with the $SrTiO_3$ layer is placed between two metal (Pt) electrodes. (b) Local density of states showing a shift of the Ti_{Sr} defect state depending on the polarization state.

DOI: 10.1021/acs.nanolett.7b04444
Nano Lett. 2018, 18, 491−497

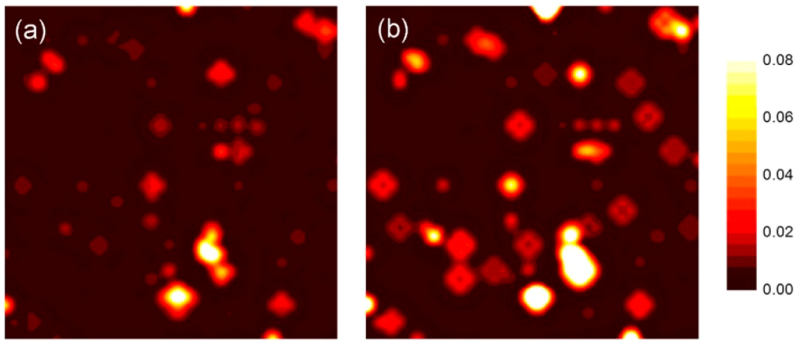

Figure 4. Polarization-dependent tunneling transmission distribution in the $SrTiO_3$ film with (a) upward, and (b) downward polarization states calculated using a tight-binding model on a 40 × 40 transverse lattice with random distribution of defects.

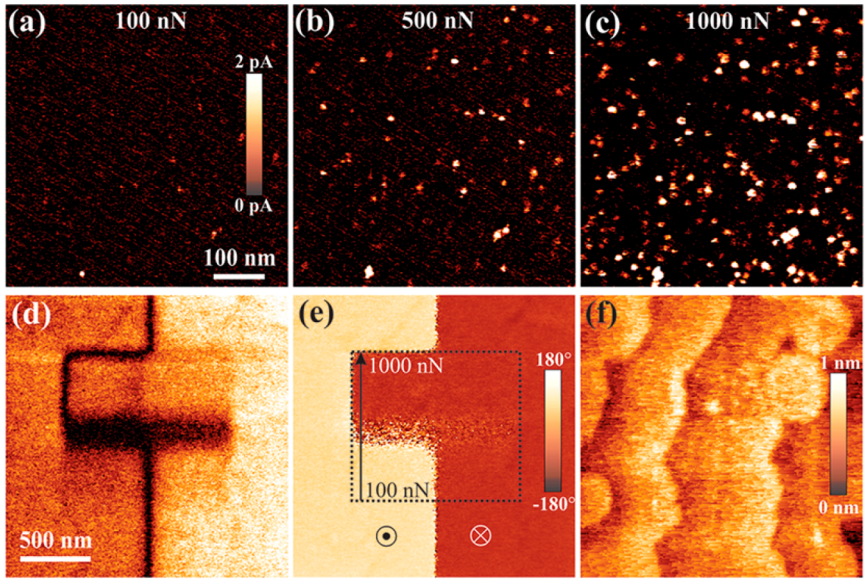

Figure 5. Mechanical control of the "hot spots" density and conductivity in the 12 u.c. thick $SrTiO_3$ film. (a–c) C-AFM images acquired while scanning the film with the tip under (a) 100, (b) 500, and (c) 1000 nN mechanical load. A density of the "hot spots" increases with increase in the mechanical load. (d,e) PFM amplitude (d) and phase (e) images of a bipolar domain structure where the central 1 × 1 μm^2 area (marked with a dashed square in (e)) has been mechanically switched. The mechanical load was increased from 100 to 1000 nN in the bottom-up direction. (f) AFM topographic image acquired after mechanical switching showing no surface damage.

the defects states shift in energy. For the P_{up} polarization direction, the defect state lies below the Fermi energy, whereas for the P_{down} polarization direction, this state shifts up in energy by about 0.13 eV and overlaps the Fermi energy. A higher conductance is, therefore, expected in the latter case due to resonant tunneling.

We note that asymmetry in the conductance for opposite polarization directions can be caused not only by the position of the defects states but also by the presence of an intrinsic electric field in the FTJs due to the different work functions of the two electrodes. In this case, the Ti_{Sr} defect states in $SrTiO_3$ near one interface are closer to the Fermi energy than the defect states near an opposite interface. In order to capture this behavior and address (iii) above, we performed tight-binding calculations of the conductance distribution over a thin ferroelectric insulating barrier layer placed on a semi-infinite metal electrode. The electronic structure of the metal and the ferroelectric with defects was designed to qualitatively reproduce the results of our first-principles modeling (see Materials and Methods for details). Figure 4 shows representative results for the transmission distribution for the upward and downward polarization states of the ferroelectric barrier. Out of several randomly distributed defects states only those close to Fermi level lead to high transmission, resulting in hot spots. Conductivity of these hot spots is polarization-dependent as the electrostatic potential for the downward (upward) polarization shifts the defect states closer to (farther from) the Fermi energy. As a result, the transmission for the upward polarization is suppressed (Figure 4a) while transmission for the downward polarization is enhanced (Figure 4b). This behavior is qualitatively similar to our experimental observations, indicating that the resonant tunneling mechanism associated with the intrinsic defects in $SrTiO_3$ is responsible for the polarization-dependent hot spot pattern of the conductance distribution. We note that the presence of localized states in the barrier layer may lead to the nonlinear $I-V$ characteristics due to resonant tunneling similar to those seen in Figure 1f.

We also found that in addition to the electrical control, resistive switching of the conductive channels in $SrTiO_3$ could be tuned by application of the mechanical force. The advantage of this approach is that it alleviates problems associated with the electrochemical modification of the surface and induced

DOI: 10.1021/acs.nanolett.7b04444
Nano Lett. 2018, 18, 491–497

conductivity due to filament formation. A set of the C-AFM images in Figure 5a–c obtained by scanning the $SrTiO_3$ film with the tip under different mechanical loads during imaging clearly demonstrate that an increasing tip-induced pressure generates a larger density of hot spots and also makes them more conducting. The induced conductive paths remain intact even after the mechanical load is released (Figure S4 in Supporting Information). This phenomenon can be explained by mechanically induced polarization switching in the $SrTiO_3$ films due to the flexoelectric effect resulting from the tip-induced stress gradient.[16−18] The PFM images illustrating the mechanical switching of polarization, which were acquired after mechanical scanning, are shown in Figure 5d,e. It can be seen that scanning over a 1×1 μm^2 area of the bipolar domain structure with the electrically grounded AFM tip under an incrementally increasing load (from 100 to 1000 nN) leads to an inversion of the PFM phase contrast in the left half of the image in Figure 5e from bright to dark at a load of about 500 nN indicating reversal of the polarization from up to down. Note that the film surface did not exhibit any sign of permanent damage after scanning with high mechanical load (Figure 5f). Phase-field simulations confirm the flexoelectric mechanism of mechanically induced switching of the polar nanoregions (PNRs) existing in the $SrTiO_3$ films (Figure S5 in Supporting Information).

The proposed mechanism of resistive switching in thin films of $SrTiO_3$ is different from that previously reported for bulk $SrTiO_3$ single crystals,[9] where the filamentary conduction occurs due to local modulations of the oxygen content. The magnitude of current in hot spots observed here for 12 u.c. thick films of $SrTiO_3$ is smaller by a factor of 10^3 than the current reported in the bulk $SrTiO_3$ single crystals.[9] Furthermore, our C-AFM data show that both the hot spot density and the current density decrease exponentially with increasing $SrTiO_3$ film thickness (Figure S1), which is not expected for bulk samples. This behavior is consistent with the results of our tight-binding modeling, which assumes a random distribution of point defects over the volume of an insulating layer serving as a barrier between the tip and the bottom electrode (Figure S2). Also, mechanically induced resistive switching is a voltage-free process, which excludes the electrochemistry-mediated mechanism of conduction enhancement, such as the formation of conducting filaments. All this evidence suggests that defect-assisted tunneling mechanism, where the conduction is dominated by "hopping" through a defect state,[15] plays a decisive role in thin film $SrTiO_3$ samples. Our experimental and theoretical results showing the polarization-dependent conductance of the hot spots (Figures 1–4) are consistent with the polar defect nature of the ferroelectric polarization in $SrTiO_3$. Although other kinds of nonpolar defects in $SrTiO_3$,[11,12] such as oxygen vacancies, may also contribute to the conduction, the effect of ferroelectric polarization on their energy position is likely to be weaker.

Overall, our results demonstrate that the resistive switching behavior of the strain-free ultrathin $SrTiO_3$ films is controlled by the formation of the conducting paths, hot spots, at the locations of the Ti_{Sr} antisite defects, which are also responsible for the appearance of polar nanoregions and emergence of the net ferroelectric polarization. We suggest that the origin of the hot spots is resonant tunneling through the localized electronic states created in the band gap of $SrTiO_3$ due to the Ti_{Sr} antisite defects. Additional measurements may be necessary to corroborate this mechanism. It is shown that the energy position of the localized defect states can be modulated by ferroelectric polarization, leading to the polarization-dependent conductance of the hot spots. Polarization-controlled defect-assisted tunneling manifests a new mechanism of resistive switching in oxide heterostructures. In addition, the conductivity of the hot spots can be modulated by mechanical stress, opening a possibility for development of conceptually new electronic devices with mechanically tunable resistive states.

Materials and Methods. *Thin Film Growth.* Strain-free $SrTiO_3$ epitaxial thin films were grown on (001) $SrTiO_3$ substrate using the pulsed laser deposition (PLD) method.[19] Before deposition, low miscut (<0.05°) $SrTiO_3$ substrates were etched with a buffered hydrofluoric acid for 1 min and annealed in oxygen at 1050 °C for 6 h to create atomically smooth single TiO_2-terminated surfaces with unit cell steps. A $SrRuO_3$ layer with a thickness of 10–15 nm was deposited as a bottom electrode on the $SrTiO_3$ substrate. A KrF excimer laser (248 nm) beam was focused on stoichiometric $SrRuO_3$ ceramic and $SrTiO_3$ single-crystal targets to an energy density of ~2.0 J/cm^2 and pulsed at 3–5 Hz. $SrTiO_3$ films were grown at a substrate temperature of 750 °C and oxygen partial pressures of 10 mTorr. The PLD system was equipped with high-pressure reflection high-energy electron diffraction, which enabled atomic layer controlled growth and in situ monitoring during the growth. After growth, the films were slowly cooled to room temperature in 1 atm of oxygen.

PFM and C-AFM Imaging. PFM and C-AFM measurements were performed using on a commercial AFM system (Asylum Research, MFP3D). Pt-coated Si tips (PPP-EFM, Nanosensors) were used for PFM and C-AFM imaging. For PFM imaging, a resonant-enhanced mode was used with resonance frequency around 350 kHz and ac modulation amplitude of 0.3 V. For C-AFM imaging, a constant dc bias of 1 V was applied to the bottom electrode, whereas the tip was grounded. The resolution for measured current was around 0.1 pA.

Density Functional Theory Calculations. Density functional theory (DFT) calculations were performed using a model system of a periodic 2×2 supercell of $Pt/(SrTiO_3)_5/Pt$ (001) with a single Ti_{Sr} defect. For simplicity, we assumed identical Pt electrodes and an energetically favorable TiO_2 interface termination of the $SrTiO_3$. The in-plane lattice constant of the supercell was constrained to the bulk lattice constant of $SrTiO_3$ a = 3.903 Å. The atomic and electronic structure of the system was calculated using the plane-wave DFT methodology as implemented in the Vienna Ab Initio Simulation Package (VASP) code.[20] We employed the Perdew–Burke–Ernzerhof (PBE) exchange-correlation functional[21] in the modified form for solids (PBEsol)[22] within the generalized gradient approximation (GGA) in combination with the projector augmented wave (PAW) potentials.[23] On-site electron–electron Coulomb interactions of the Ti-3d states were treated within the GGA + U approach with U_{eff} = 4.36 eV. Calculations were carried out using plane-wave basis set with a cutoff kinetic energy of 400 eV and $6 \times 6 \times 1$ mesh of k points in the irreducible Brillouin zone until the total energy was converged to within 0.01 meV per cell. Atomic relaxations were performed until the Hellmann–Feynman forces on atoms were less than 20 meV/Å.

Tight-Binding Modeling. The transmission coefficient was calculated using the tight-binding (TB) Green's function technique.[24] A single-band TB model on a cubic lattice with a nearest-neighbor hopping parameter t was used in the

DOI: 10.1021/acs.nanolett.7b04444
Nano Lett. 2018, 18, 491–497

calculations (a representative value of t is 1 eV). The top "scanning-probe" electrode was modeled by the 1D atomic chain with on-site energy $\varepsilon_L = -t$. The insulating barrier layer and the bottom electrode had a finite cross section of $N_x \times N_y$ sites. The on-site atomic energies of the insulating layer, the defect atoms, and the bottom electrode were taken to be $\varepsilon_B = 6.5t$, $\varepsilon_D = -5.88t$, and $\varepsilon_R = 3.0t$, respectively. The Fermi energy was assumed to be $E_F = 0$. These parameters place the conduction band minimum $3t$ below E_F for the bottom and top electrodes and $0.5t$ above E_F for the insulator. The resulting resonant state appears at about $-0.5t$ (which is consistent with our first-principles results for $t = 1$ eV). The intrinsic potential drop due to the difference in the work functions of the electrodes, ΔU, and the potential drop due to the ferroelectric polarization ΔV_P are considered as parameters. In particular calculations shown in Figure 4, they are assumed to be $\Delta U = 0.25t$ and $\Delta V_P = \pm 0.2t$. Other parameters used in this calculation are as follows: $N_x = N_y = 40$ u.c. and insulator layer thickness is $d = 4$ u.c. Ten percent of defect states were considered to be randomly distributed within the ferroelectric barrier layer.

Phase-Field Modeling. The phase-field model for $SrTiO_3$ (STO) films with polar nanoregions (PNR) follows our previous work.[10] The temporal evolution of polarization is described by the time-dependent Ginzburg–Landau (TDGL) equation, that is

$$\frac{\partial P(x, t)}{\partial t} = -L\frac{\delta F}{\delta P(x, t)}$$

where $P(x, t)$ is the polarization at position x at time step t, F is the total free energy density and L is the kinetic coefficient related to domain wall mobility. The bulk, elastic, electric, flexoelectric, and gradient energy contributions are considered in the total free energy F, which is expressed as

$$F = \iiint_V [f_{Bulk}(P_i) + f_{Electric}(P_i, E_i) + f_{Elastic}(P_i, \varepsilon_{ij}) + f_{Flexo}(P_i, \varepsilon_{ij}) + f_{gradient}(P_{i,j})]dx^3$$

The detailed expression for each term is elucidated in our previous works.[25−27] The parameters used in the total free energy of STO in this work are the same as Li et al's work[28] and the flexocoupling coefficients from Zubko et al's measurements,[29,30] that is, $f_{11} = 0.08$ V, $f_{12} = 2.6$ V, and $f_{44} = 2.2$ V. For the PNR region of STO, the coefficients in the Landau bulk energy is modified to fit the equilibrium polarization along {001} as ~0.1 C/m^2 calculated by previous DFT calculations.[10] The PNR is set to be at the center of STO film with a spherical shape of 15 nm in diameter.

To solve the three-dimensional TDGL equation of polarization, the system is discretized into $128\Delta x \times 128\Delta x \times 40\Delta x$ with grid size $\Delta x = 0.39$ nm. Semi-implicit Fourier transformation method is used.[31] Periodical boundaries are assumed laterally and the lateral size is chosen to be large enough to eliminate the interactions between PNR with its images. Along the x_3 direction, the system is divided into substrate, film and air in the, where each part takes up 20, 12, and 8 Δx, respectively. A free boundary condition, that is, $\frac{\partial P_3}{\partial x_3} = 0$, is assumed for polarization. The routines for solving the elastic and electric equations were well described in refs 25 and 26. To mimic the probe force, a hyperbolic tangent function is assumed to approximate the stress distribution on the film surface and superimposed on the stress-free boundary condition at the top surface. The short circuit electric boundary condition is adopted for both top and bottom interfaces to represent a fully compensated film. The system is first poled by 1 V bias from a uniform top electrode for enough long time to reach equilibrium. Then it is subjected to an incremental mechanical force imposed at the center of PNR region on the film surface. The loading forces increase from 200 up to 1000 nN with an increment of 100 nN/2000 timesteps. Finally the force is removed and the system is let to relax to the equilibrium.

■ ASSOCIATED CONTENT

Supporting Information

The Supporting Information is available free of charge on the ACS Publications website at DOI: 10.1021/acs.nanolett.7b04444.

Additional information, figures, and refs (PDF)

■ AUTHOR INFORMATION

Corresponding Authors

*(V.A.) E-mail: valexandrov2@unl.edu.
*(C.B.E.) E-mail: ceom@wisc.edu.
*(A.G.) E-mail: agruverman2@unl.edu.

ORCID

Konstantin Klyukin: 0000-0001-8325-8725
Alexei Gruverman: 0000-0003-0492-2750

Author Contributions

H.L. and D.L contributed equally to the project. H.L., D.L., E.Y.T., C.B.E., and A.G. designed the research. H.L. carried out the PFM and C-AFM measurements; D.L., H.L., and J. L. fabricated thin film samples; K.K., L.T., T.R.P, E.Y.T., and V.A. performed DFT calculations and tight-binding calculations; B.W. and L.Q.C. performed phase-field modeling. All the authors contributed to the manuscript preparation.

Notes

The authors declare no competing financial interest.

■ ACKNOWLEDGMENTS

This work was supported by the National Science Foundation (NSF) through Materials Research Science and Engineering Center (MRSEC) under Grant DMR-1420645. K.K., T.R.A., E.T., and V.A. acknowledge the Holland Computing Center at the University of Nebraska-Lincoln for providing computational resources. Work at the University of Wisconsin was supported by funding from the DOE Office of Basic Energy Sciences under award number DE-FG02-06ER46327. This research used resources of the National Energy Research Scientific Computing Center, a DOE Office of Science User Facility supported by the Office of Science of the U.S. Department of Energy under Contract No. DE-AC02-05CH11231. B.W. was funded by the Penn State MRSEC, Center for Nanoscale Science, under the award NSF DMR-1420620. L.Q.C. acknowledges NSF DMREF support under Grant DMR1629270.

■ REFERENCES

(1) Waser, R.; Aono, M. Nanoionics-based resistive switching memories. *Nat. Mater.* **2007**, *6*, 833−840.

DOI: 10.1021/acs.nanolett.7b04444
Nano Lett. 2018, 18, 491−497

(2) Jeong, D. S.; Thomas, R.; Katiyar, R. S.; Scott, J. F.; Kohlstedt, H.; Petraru, A.; Hwang, C. S. Emerging memories: resistive switching mechanisms and current status. *Rep. Prog. Phys.* **2012**, *75*, 076502.
(3) Ielmini, D. Resistive switching memories based on metal oxides: mechanisms, reliability and scaling. *Semicond. Sci. Technol.* **2016**, *31*, 063002.
(4) Lee, M. H.; Hwang, C. S. Resistive switching memory: observations with scanning probe microscopy. *Nanoscale* **2011**, *3*, 490−502.
(5) Waser, R.; Dittmann, R.; Staikov, G.; Szot, K. Redox-Based Resistive Switching Memories − Nanoionic Mechanisms, Prospects, and Challenges. *Adv. Mater.* **2009**, *21*, 2632−2663.
(6) Gruverman, A.; Wu, D.; Lu, H.; Wang, Y.; Jang, H. W.; Folkman, C. M.; Zhuravlev, M. Y.; Felker, D.; Rzchowski, M.; Eom, C.-B.; Tsymbal, E. Y. Tunneling electroresistance effect in ferroelectric tunnel junctions at the nanoscale. *Nano Lett.* **2009**, *9*, 3539−3543.
(7) Garcia, V.; Fusil, S.; Bouzehouane, K.; Enouz-Vedrenne, S.; Mathur, N. D.; Barthélémy, A.; Bibes, M. Giant tunnel electroresistance for non-destructive readout of ferroelectric states. *Nature* **2009**, *460*, 81−84.
(8) Tsymbal, E. Y.; Gruverman, A.; Garcia, V.; Bibes, M.; Barthélémy, A. Ferroelectric and Multiferroic Tunnel Junctions. *MRS Bull.* **2012**, *37*, 138−143.
(9) Szot, K.; Speier, W.; Bihlmayer, G.; Waser, R. Switching the electrical resistance of individual dislocations in single-crystalline $SrTiO_3$. *Nat. Mater.* **2006**, *5*, 312−320.
(10) Lee, D.; Lu, H.; Gu, Y.; Choi, S.-Y.; Li, S.-D.; Ryu, S.; Paudel, T. R.; Song, K.; Mikheev, E.; Lee, S.; Stemmer, S.; Tenne, D. A.; Oh, S. H.; Tsymbal, E. Y.; Wu, X.; Chen, L.-Q.; Gruverman, A.; Eom, C. B. Emergence of room-temperature ferroelectricity at reduced dimensions. *Science* **2015**, *349*, 1314−1317.
(11) Choi, M.; Oba, F.; Tanaka, I. Role of Ti antisite-like defects in $SrTiO_3$. *Phys. Rev. Lett.* **2009**, *103*, 185502.
(12) Klyukin, K.; Alexandrov, V. Effect of intrinsic point defects on ferroelectric polarization behavior of $SrTiO_3$. *Phys. Rev. B: Condens. Matter Mater. Phys.* **2017**, *95*, 035301.
(13) Larkin, A. I.; Matveev, K. A. Current-voltage characteristics of mesoscopic semiconductor contacts. *Sov. Phys. JETP* **1987**, *66*, 580−584.
(14) Klaua, M.; Ullmann, D.; Barthel, J.; Wulfhekel, W.; Kirschner, J.; Urban, R.; Monchesky, T. L.; Enders, A.; Cochran, J. F.; Heinrich, B. Growth, structure, electronic, and magnetic properties of MgO/Fe(001) bilayers and Fe/MgO/Fe(001) trilayers. *Phys. Rev. B: Condens. Matter Mater. Phys.* **2001**, *64*, 134411.
(15) Tsymbal, E. Y.; Pettifor, D. G. Spin-polarized electron tunneling across a disordered insulator. *Phys. Rev. B: Condens. Matter Mater. Phys.* **1998**, *58*, 432.
(16) Lu, H.; Bark, C.-W.; Esque de los Ojos, D.; Alcala, J.; Eom, C. B.; Catalan, G.; Gruverman, A. Mechanical Writing of Ferroelectric Polarization. *Science* **2012**, *336*, 59−61.
(17) Očenášek, J.; Lu, H.; Bark, C. W.; Eom, C. B.; Alcalá, J.; Catalan, G.; Gruverman, A. Nanomechanics of Flexoelectric Switching. *Phys. Rev. B: Condens. Matter Mater. Phys.* **2015**, *92*, 035417.
(18) Lu, H.; Wang, B.; Li, T.; Lipatov, A.; Lee, H.; Rajapitamahuni, A.; Xu, R.; Hong, X.; Farokhipoor, S.; Martin, L. W.; Eom, C.-B.; Chen, L.-Q.; Sinitskii, A.; Gruverman, A. Nanodomain Engineering in Ferroelectric Capacitors with Graphene Electrodes. *Nano Lett.* **2016**, *16*, 6460−6466.
(19) Eom, C. B.; Cava, R. J.; Fleming, R. M.; Phillips, J. M.; van Dover, R. B.; Marshall, J. H.; Hsu, J. W. P.; Krajewski, J. J.; Peck, W. F., Jr. Single-crystal epitaxial thin films of the isotropic metallic oxides $Sr_{1-x}Ca_xRuO_3$. *Science* **1992**, *258*, 1766.
(20) Kresse, G.; Furthmüller, J. Efficient Iterative Schemes for *Ab Initio* Total-Energy Calculations Using a Plane-Wave Basis Set. *Phys. Rev. B: Condens. Matter Mater. Phys.* **1996**, *54*, 11169.
(21) Perdew, J. P.; Burke, K.; Ernzerhof, M. Generalized Gradient Approximation Made Simple. *Phys. Rev. Lett.* **1996**, *77*, 3865.
(22) Perdew, J. P.; Ruzsinszky, A.; Csonka, G. I.; Vydrov, O. A.; Scuseria, G. E.; Constantin, L. A.; Zhou, X.; Burke, K. Restoring the Density-Gradient Expansion for Exchange in Solids and Surfaces. *Phys. Rev. Lett.* **2008**, *100*, 136406.
(23) Blöchl, P. E. Projector Augmented-Wave Method. *Phys. Rev. B: Condens. Matter Mater. Phys.* **1994**, *50*, 17953.
(24) Datta, S. *Electronic Transport in Mesoscopic Systems*; Cambridge University Press: Cambridge, U.K., 1995.
(25) Li, Y. L.; Hu, S. Y.; Liu, Z. K.; Chen, L. Q. Effect of Electrical Boundary Conditions on Ferroelectric Domain Structures in Thin Films. *Appl. Phys. Lett.* **2002**, *81*, 427.
(26) Li, Y. L.; Hu, S. Y.; Liu, Z. K.; Chen, L. Q. Effect of Substrate Constraint on the Stability and Evolution of Ferroelectric Domain Structures in Thin Films. *Acta Mater.* **2002**, *50*, 395−411.
(27) Gu, Y. J.; Hong, Z. J.; Britson, J.; Chen, L.-Q. Nanoscale mechanical switching of ferroelectric polarization via flexoelectricity. *Appl. Phys. Lett.* **2015**, *106*, 022904.
(28) Li, Y. L.; Choudhury, S.; Haeni, J. H.; Biegalski, M. D.; Vasudevarao, A.; Sharan, A.; Ma, H. Z.; Levy, J.; Gopalan, V.; Trolier-McKinstry, S.; Schlom, D. G.; Jia, Q. X.; Chen, L. Q. Phase transitions and domain structures in strained pseudocubic (100) $SrTiO_3$ thin films. *Phys. Rev. B: Condens. Matter Mater. Phys.* **2006**, *73*, 184112.
(29) Zubko, P.; Catalan, G.; Buckley, A.; Welche, P. R. L.; Scott, J. F. Strain-Gradient-Induced Polarization in $SrTiO_3$ Single Crystals. *Phys. Rev. Lett.* **2007**, *99*, 167601.
(30) Zubko, P.; Catalan, G.; Tagantsev, A. K. Flexoelectric Effect in Solids. *Annu. Rev. Mater. Res.* **2013**, *43*, 387−421.
(31) Chen, L. Q.; Shen, J. Applications of Semi-Implicit Fourier-Spectral Method to Phase Field Equations. *Comput. Phys. Commun.* **1998**, *108*, 147−158.

DOI: 10.1021/acs.nanolett.7b04444
Nano Lett. 2018, 18, 491−497